Chapter 16
Capture of Thin Film Vibromorphology using Laser Vibrometry and Frequency-Domain Viscoelastic Vibroacoustics

Kent X. Eng, Steven Kao, Natalie J. White, Nakul Deshpande, Jeffery D. Tippmann, and Eric C. Bryant

Abstract Applications of thin film vibromorphology are increasingly relevant because of the emergent use of engineered polymers for device design (*e.g.*, of Triboelectric Nanogenerators (TENGs)). Modern research applications of thin-film technology like TENGs focus on harvesting mechanical energy for power generation or sensing technologies. However, there is an existing research gap in the numerical and experimental investigation of thin film vibromorphology that compliments design efforts for modern technological applications.

To address this gap, the present work presents a combined experimental and numerical investigation of the vibroacoustics of thin polymer films. The vibroacoustic morphology (*i.e.*, so-called "vibromorphology") of one-or-more contacting thin polymer films during deformation under acoustic excitation is characterized. Specifically, variations in experimental frequency response curves (FRCs) under the films' structural-dynamics parameterization (*viz.*, a considered subset of influence from size, initial tensioning, thickness, multiplicity, etc.) are described via a combination of experimental and numerical methods.

In doing so, experimental optical inference of the films' viscoelastic deformations under acoustic excitation via 3D laser vibrometry is complimented with finite element analysis (FEA) of the films' structural dynamics. Influence of the films' geometry and fixture (*e.g.*, film size and initial tensioning) are described by modification of numerical mesh and material data. Novel FEA-based simulation methods for film contact are exercised, particularly with regard to treatment of FEA as a forward problem for material data inversion.

Keywords Film vibromorphology · Finite element analysis (FEA) · Laser vibrometry · Model validation · Optimization

Kent X. Eng · Steven Kao · Natalie J. White
National Security Education Center (NSEC), Los Alamos National Laboratory, Los Alamos, NM 87545
e-mail: kente@lanl.gov; tundra@lanl.gov; njwhite@lanl.gov

Kent X. Eng
Department of Civil and Environmental Engineering, Princeton University, Princeton, NJ 08544
e-mail: kente@lanl.gov

Steven Kao
Department of Electrical and Computer Engineering, The University of New Mexico, Albuquerque, NM 87131
e-mail: tundra@lanl.gov

Natalie J. White
Department of Mechanical Engineering, Brigham Young University, Provo, UT 84602
e-mail: njwhite@lanl.gov

Nakul Deshpande · Eric C. Bryant
National Security Earth Science (EES-17), Los Alamos National Laboratory, Los Alamos, NM 87545
e-mail: njwhite@lanl.gov ; ecbryant@lanl.gov

Jeffery D. Tippmann
Space Remote Sensing and Data Science (ISR-6), Los Alamos National Laboratory, Los Alamos, NM 87545
e-mail: jtippmann@lanl.gov

Janko Slavic et al. (eds.), *Computer Vision & Laser Vibrometry, Vol. 6*, Conference Proceedings of the Society for Experimental Mechanics Series, https://doi.org/10.13052/97887-438-0151-1_16

Introduction

Triboeletic Nanogenerators (TENGs) comprise a new mechanical energy harvesting technology based on contact electrification and electrostatic induction. TENGs are a multi-thin-flim system: a parallel-plate capacitor formed between a tribocharged dielectric material surface and two electrode materials [1]. When a TENGs vibrates, opposed surfaces are understood to experience effective charge polarization inducing electric discharge at the electrodes; charge strength/polarity yielded depends on material properties, straining, temperature, *etc.* [2]. Resurgent interest in applications of thin film vibromorphology is motivated by the emergence of engineered polymers in TENG design [3, 4] for: harvesting mechanical energy for power generation [5, 6] and use in sensor technologies [7, 8], among other applications. Currently, a research gap exists in experimental and numerical investigation of multi-layer polymer, thin-film vibromorphology for engineering design of TENG devices.

In this work, measurements are designed to enable *separately tensioned* thin films to be tested (1) *individually*, (2) *in proximity*, and (3) *in contact* to describe vibromorphological sensitivity. In addition, our numerical work establishes a principled approach to characterize multi-thin-film deformation during so-called "*en echelon*" contact under frequency-domain Finite Element Analysis (FEA). Complicating this task, manufacturer-provided polymer properties may be unreliable due to inconsistent manufacturing processes (*i.e.*, batch variability [9]) and/or infeasibility of standard testing regimes due to specimen thinness. As such, the additional challenge of inverse methods for film flexural parameters is also addressed.

Research Objectives

To address the research gap identified above, our current procedure combines experimental and numerical investigation of thin polymer films' vibroacoustic morphology. Our work provides:

- Vibroacoustic experimentation to quantify impact of thin films' initial tensioning, multiplicity, and/or contact distance
- Numerical simulation of thin films' vibroacoustic excitement via frequency-domain FEA
- Optimization-based method for inference from thin films' structural dynamics
- Integrated framework of experimental, FEA-based, and optimization methods to infer thin films' flexural properties

Substantive prior research has been undertaken to address experimental/numerical challenges of TENG design, as indicated above, and is now distinguished from the present work. In addition, our unique research emphasis is identified: development of an analysis framework to integrate experimental and numerical results of multi-layer-film vibromorphology.

Research Background

Thin polymers, as used in TENG design, are nonstructural materials and manufactured absent a codified standard for flexural material performance. As a consequence, flexural material properties – Young's modulus, E, Poisson's Ratio, ν, *etc.* – can differ significantly between samples due to batch variability [9]. Moreover, standard evaluation methods may fail because of the films' compliance to out-of-plane deformation. To address this issue, later nondestructive methods in membrane dynamics [10, 11, 12] and frequency spectra [13] have been introduced. Our novel contribution is to describe multi-layer polymers' vibromorphology with respect to (abbreviated "w.r.t.") unstudied characteristics like film tensioning – ultimately, with the aim to improve TENG operational efficiency by tuning to specific natural frequencies [13].

Laser Doppler Vibrometry (LDV), a nondestructive testing method, is used in our thin-film dynamics analysis due to its advantage of detecting resonant out-of-plane motion [14]. Extant LDV methods for resonant frequency analysis focus on a single layer [12, 15] or clamped multi-layers [16]. Experimentation on clamped multi-layers with engineering initial tensioning is outside the present literature, with current state-of-art for initial tensioning remaining single-layer [17, 18]. In this work, testing is conducted on multi-layer polymers with separate clamping on each layer: the layers may be tested separately, together, and in presence or absence of tensioning. In addition, our experimentation incorporates improved multi-layer-film fixtures – *i.e.*, new composite film "holders" – enabling vibrometry under parameterization of contact distance.

Mathematical Description

Researchers have developed diverse FEA strategies to model the behavior of single thin films, such as elastic modulus, residual stress [17], and channel cracking [19], *etc.* However, frequency-domain FEA for multi-layer polymer assemblages is less broad, particularly if layer interfaces are understood as potential sites of viscous dissipation (as here). Researchers have developed other FEA methods for TENGs, focusing mainly on sliding-mode theory [20], topology modeling [21], and electrostatic behavior [22]. There is a research gap on FEA for dynamic interactions between polymer films – particularly combined with experiential determinations on the applicability of frequency-domain analysis.

In-line with [23], a variational principle for frequency-domain structural analysis incorporating effects of *en echelon* structure-structure interaction is developed. The material under investigation is viscoelastic. Thus, the time-domain stress and strain tensors and displacement vector will be complex-valued fields. Under cyclic loading with frequency ω at time t, these fields are described by the mapping:

$$\tilde{\boldsymbol{\sigma}} = \boldsymbol{\sigma}\, e^{i\omega t} \quad \text{(stress)} \tag{1}$$

$$\tilde{\boldsymbol{\epsilon}} = \boldsymbol{\epsilon}\, e^{i\omega t} \quad \text{(strain)} \tag{2}$$

$$\tilde{\boldsymbol{u}} = \boldsymbol{u}\, e^{i\omega t} \quad \text{(displacement)} \tag{3}$$

where the real parts of fields $\tilde{\boldsymbol{\sigma}}, \tilde{\boldsymbol{\epsilon}}, \tilde{\boldsymbol{u}}$ approximate the actual material state. Time-independent fields $\boldsymbol{\sigma}, \boldsymbol{\epsilon}, \boldsymbol{u}$ are likewise complex-valued, with displacement $\boldsymbol{u}$ ultimately discretized as the solution vector for frequency-domain FEA.

Multi-Body Potential

The above notation is now generalized to a two-body assemblage. A complex-valued displacement vectorfield, $\boldsymbol{u}_\alpha \in \mathbb{C}^3$, is restricted to the primary solid domain, $\mathscr{B}_\alpha \subseteq \mathbb{R}^3$. The displacement vectorfield, $\boldsymbol{u}_\beta \in \mathbb{C}^3$, is likewise restricted to a secondary solid domain, $\mathscr{B}_\beta \subseteq \mathbb{R}^3$. Under isothermal conditions, this variational principle is

$$\Phi(\boldsymbol{u}_\alpha, \boldsymbol{u}_\beta) = \Phi_\alpha(\boldsymbol{u}_\alpha) + \Phi_\beta(\boldsymbol{u}_\beta) + \Phi_{\alpha\beta}(\boldsymbol{u}_\alpha, \boldsymbol{u}_\beta) \tag{4}$$

where the solid continuum terms are

$$\Phi_\iota(\boldsymbol{u}_\iota) = \int_{\mathscr{B}_\iota} (U_\iota - K_\iota)\mathrm{d}V - \int_{\partial \mathring{\mathscr{B}}_\iota} u_{\iota\, i} \mathring{S}_{\iota\, ij} n_j \mathrm{d}S, \quad \iota = \alpha, \beta \tag{5}$$

with $\mathring{S}_{\iota\, ij} n_j$ prescribed on boundaries $\partial \mathring{\mathscr{B}}_\iota$ for $\iota = \alpha, \beta$. On each of $\mathscr{B}_\alpha$ and $\mathscr{B}_\beta$, nonsymmetric second-order stress tensor $\boldsymbol{S}_\iota$ is

$$\boldsymbol{S}_\iota = \frac{\partial U_\iota}{\partial \nabla \boldsymbol{u}_\iota} = \underbrace{\frac{\partial U_\iota}{\partial \boldsymbol{\epsilon}_\iota}}_{=\boldsymbol{\sigma}_\iota} : \frac{\partial \boldsymbol{\epsilon}_\iota}{\partial \nabla \boldsymbol{u}_\iota}, \quad \iota = \alpha, \beta \tag{6}$$

where $\boldsymbol{\sigma}_\iota$ and $\boldsymbol{\epsilon}_\iota$ are symmetric static and kinematic tensors, respectively.

Inter-Body Potential

The interface coupling term specifies *en echelon* motion via the particularization:

$$\Phi_{\alpha\beta}(\boldsymbol{u}_\alpha, \boldsymbol{u}_\beta) = \int_{\partial \mathscr{B}_{\alpha\beta}} \left(\frac{k_N^*}{2} [\![u]\!]_{N\, i} [\![u]\!]_{N\, i} + \frac{k_T^*}{2} [\![u]\!]_{T\, i} [\![u]\!]_{T\, i} \right) \mathrm{d}S = \Phi_{\beta\alpha}(\boldsymbol{u}_\alpha, \boldsymbol{u}_\beta) \tag{7}$$

for total, normal, and tangential jump quantities given, respectively, by

$$[\![\boldsymbol{u}]\!]_{\alpha\beta} = \boldsymbol{u}_\beta - \boldsymbol{u}_\alpha, \quad [\![\boldsymbol{u}]\!]_N|_{\partial \mathscr{B}_{\alpha\beta}} = \boldsymbol{N}|_{\partial \mathscr{B}_{\alpha\beta}} \cdot [\![\boldsymbol{u}]\!]_{\alpha\beta}, \quad [\![\boldsymbol{u}]\!]_T|_{\partial \mathscr{B}_{\alpha\beta}} = \boldsymbol{T}|_{\partial \mathscr{B}_{\alpha\beta}} \cdot [\![\boldsymbol{u}]\!]_{\alpha\beta} = [\![\boldsymbol{u}]\!]_{\alpha\beta} - [\![\boldsymbol{u}]\!]_N|_{\partial \mathscr{B}_{\alpha\beta}}. \tag{8}$$

Second-order projections tensors $\boldsymbol{N}$ and $\boldsymbol{T}$ are such that

$$N_{ij} = n_i n_j, \qquad T_{ij} = \delta_{ij} - n_i n_j.$$

As per usual for FEA models, $\partial \mathscr{B}_{\alpha\beta}$ is described by unit outward normal $\boldsymbol{n}|_{\partial \mathscr{B}_{\alpha\beta}}$ vector from primary solid to secondary solid domain; $\partial \mathscr{B}_{\beta\alpha}$ is described by unit outward normal $\boldsymbol{n}|_{\partial \mathscr{B}_{\beta\alpha}}$ vector from secondary to primary solid domain.

Intra-Body Potential

Variations in the uncoupled potentials, $\Phi_\iota(\boldsymbol{u}_\iota)$ for $\iota = \alpha, \beta$, are now developed w.r.t. displacement vectorfield $\boldsymbol{u}_\iota$, as well as variations in the coupled potential $\Phi(\boldsymbol{u}_\alpha, \boldsymbol{u}_\beta)$. To do so, a specification of U_ι's function dependence on $\boldsymbol{\epsilon}_\iota$ is required. As for frequency-domain structural analysis, U_ι is taken as quadratic in $\boldsymbol{\epsilon}_\iota$. Consistent with [23], U_ι may be equivalently rewritten as

$$U_\iota = \frac{\lambda_\iota^*}{2}(\mathbf{1} : \boldsymbol{\epsilon}_\iota)^2 + \mu_\iota^* \boldsymbol{\epsilon}_\iota : \boldsymbol{\epsilon}_\iota = \frac{\lambda_\iota^*}{2}(\varepsilon_{\iota\, kk})^2 + \mu_\iota^* \varepsilon_{\iota\, ij}\varepsilon_{\iota\, ij}, \quad \iota = \alpha, \beta \tag{9}$$

for λ_ι^*, $\mu_\iota^* \in \mathbb{C}$ denoting the complex-valued Lame's and shear moduli. Likewise after [23], λ_ι^* and μ_ι^* may be related to common engineering measurements of complex-valued bulk and shear compliance. λ_ι^* and μ_ι^*'s real parts are the materials' real Lame's and real shear moduli; conversely, their imaginary parts likely express dependence on frequency ω. Departing from [23], K_ι is written as

$$K_\iota = \frac{\rho_\iota^* \omega^2}{2} \boldsymbol{u}_\iota \cdot \boldsymbol{u}_\iota = \frac{\rho_\iota^* \omega^2}{2} u_{\iota\, i} u_{\iota\, i}, \quad \iota = \alpha, \beta \tag{10}$$

for $\rho_\iota^* \in \mathbb{C}$ denoting the complex-valued solid density. ρ_ι^*'s real part is the solid density; conversely, its imaginary part may express dependence on frequency ω. Our departure – *i.e.*, introducing a complex-valued density – indicates: *Raleigh damping is incorporated as a specialization of complex-valued material data*.

Stationarity

Strong-form governing equations are recovered from the stationary point,

$$\underset{\boldsymbol{u}_\iota}{\delta} \left\{\Phi(\boldsymbol{u}_\alpha, \boldsymbol{u}_\beta)\right\} = 0 \;\Leftrightarrow\; S_{\iota\, ij,j} + \rho_\iota^* \omega^2 u_{\iota\, i} = 0, \tag{11}$$

as are boundary conditions given as

$$\underset{\boldsymbol{u}_\iota}{\delta} \left\{\Phi(\boldsymbol{u}_\alpha, \boldsymbol{u}_\beta)\right\} = 0 \;\Leftrightarrow\; S_{\iota\, ij} n_j|_{\partial \mathring{\mathscr{B}}_\iota} = \mathring{S}_{\iota\, ij} n_j|_{\partial \mathring{\mathscr{B}}_\iota} \text{ and } S_{ij} n_j|_{\partial \mathscr{B}_{\alpha\beta}} = (k_N^* [\![u]\!]_{N\, i} + k_T^* [\![u]\!]_{T\, i})|_{\partial \mathscr{B}_{\alpha\beta}}, \tag{12}$$

which comprise, as desired, standard prescribed traction and desired interface relations. Based on the stated variational principle, multi-thin-film FEA of interface interactions can integrate with experimental results exhibiting *en echelon* deformation.

Methods

Our overall framework forms a bridge between experimental and numerical multi-layer-film vibromorphology – by comparing measured resonant frequencies from experimental results to predicted resonant frequencies from FEA, optimized to minimize the difference thereof (Fig. 1). In each iteration of the optimization procedure, the optimizer receives predicted resonant frequencies from FEA and determines a normalized square difference from experimental measurements, a.k.a., a so-called "loss function." The optimizer then outputs an updated estimation of modal parameters, using the ADAM algorithm [24] as implemented in PyTorch. Updated parameters are used to update elastic flexural moduli used as FEA inputs, with FEA then rerun to predict resonant frequencies. This cycle repeats until the optimizer minimizes the loss function.

Experimental Procedure

LDV was used to measure the resonant frequencies of the thin films, both individually and as contacting multi-film assemblages. In particular, care is required in fixturing films for LDV due to compliance under out-of-plane deformation. To control the measurement, a circular sample of polymer was held in place with a designed fixture described in Sec. . The ring-shaped fixture clamped only the sample edges leaving the center free to vibrate, defining the boundary conditions. Fixture was clamped by fastening six screws and nuts along the perimeter. To make boundary conditions as uniform as possible, nuts were tightened using a torque wrench to the same torque value.

Once clamped in the fixture, tension could be optionally applied by attaching the "base piece." The base attached via screws and nuts in four locations. Distance between the base and clamping pieces was kept uniform by using stops or measuring with calipers. This distance governed tension applied to the sample: increased proximity of base to clamping pieces

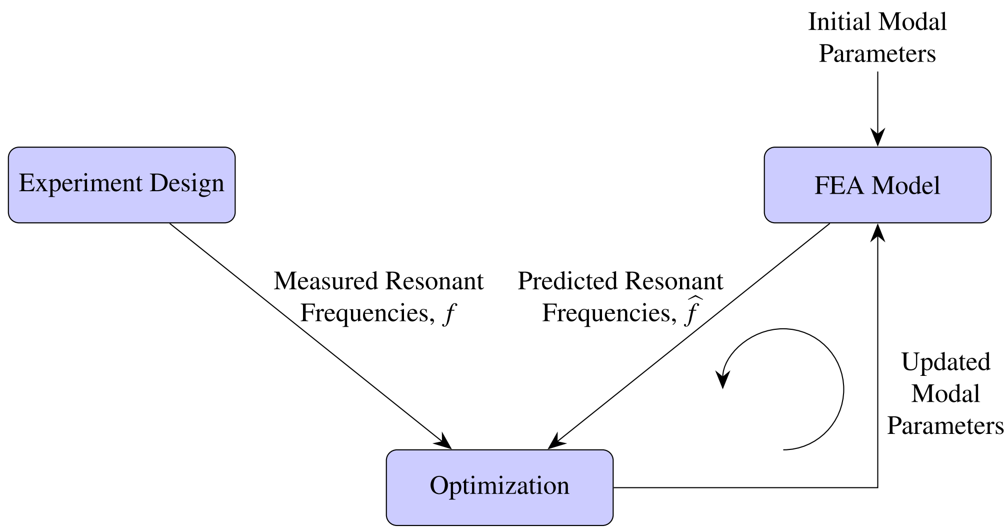

Fig. 1 Thin film model framework.

induced greater tensioning, because the tube on the base piece pressed against the sample. To avoid plastic deformation, strains of less than 2% were applied (the estimated elastic limit). Images of the sample were captured before and after tensioning for use in digital image correlation (DIC) for strain quantification, Sec. .

For testing two samples in a multi-thin-film assemblage, each sample would first be clamped and tensioned in its own fixture. Then, the two base pieces would be held together such that the samples face each other. If the samples were to be in contact, then the base pieces are clamped together with four screws at each of four tabs. If multi-thin-film samples were in close proximity, then a thin "stop" was between the tabs to create the space. Once sample(s) were secured in the fixture, fixture was held by lab clamps and oriented towards the vibrometer's laser and camera, approximately 90° to the camera view.

A nearby speaker was used as sound source for film acoustic excitation during LDV. Speaker was placed parallel to the assemblage, so that sample edges are approximately equidistant from the speaker. Speaker, along with the polymer, fixture, and LDV scanner, is shown in Fig. 2. A chirp ranging from 0-2 kHz was emitted for each scan point; this range should be reevaluated if new materials or geometries are used. LDV measured sample surface velocity at each scan point for computer data acquisition. Scan duration, usually 5 minutes or less, was determined by the number of scan points on the sample face. Data was viewed via Polytec™ software and exported for post-processing. Average sample surface velocity as a function of excitation frequency was examined for frequencies at which surface velocity peaked, which constituted the natural, or "resonant," frequencies. Coincident surface velocity distributions revealed modal shapes to confirm resonant frequencies.

Fixture Design

Two primary objectives motivated new experimental fixture design: testing films under tension and testing two films layered together. Applying tension is of interest to "tune" resonance to specific natural frequencies, which may maximize the efficiency of multi-thin-film assemblages in devices like TENGs. Additionally, measurements on multi-thin-film assemblages under contact parameterization promise similar capability for performance enhancement. A constraint was that film specimens should be clamped and tensioned independently, in order to test films separately (with or without tension) and then in contact – *viz.*, without being removed from the fixture and re-clamped. Fixture design was actuated with Polylactic Acid (PLA) 3D printing, an inexpensive and widely available manufacturing process.

Prior work [12] described a method of applying tension using a circular tube. A membrane was held in place by two rings, or flanges (similar to the aforementioned existing fixture). These two rings were moved towards a supporting back panel via threaded rods. A circular tube protruding from the back panel pressed against the membrane as the two rings moved closer to the panel, inducing tension. Fixture design implemented a similar concept from [12] by introducing a third base piece in addition to the two clamping rings: this base piece featured a circular tube with rounded edges to mitigate sample deformation. Instead of threaded rods, the base piece was penetrated by screws attaching to tabs on the lower clamping ring. Distance between base piece and clamping rings determined applied tension, *i.e.*, from tightening of screws controlled by stops.

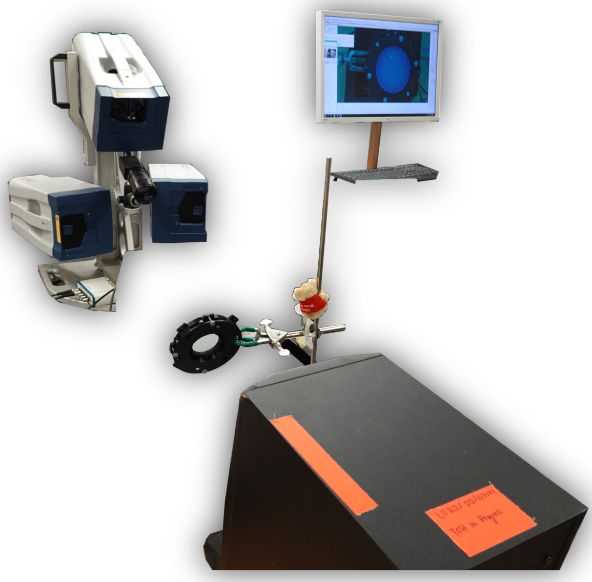

Fig. 2 Experimental set-up for LDV scans is shown. A speaker, in the foreground, provided acoustic excitation for the polymer, which is held in front of the LDV scanner. A laptop for data acquisition is in the top right corner.

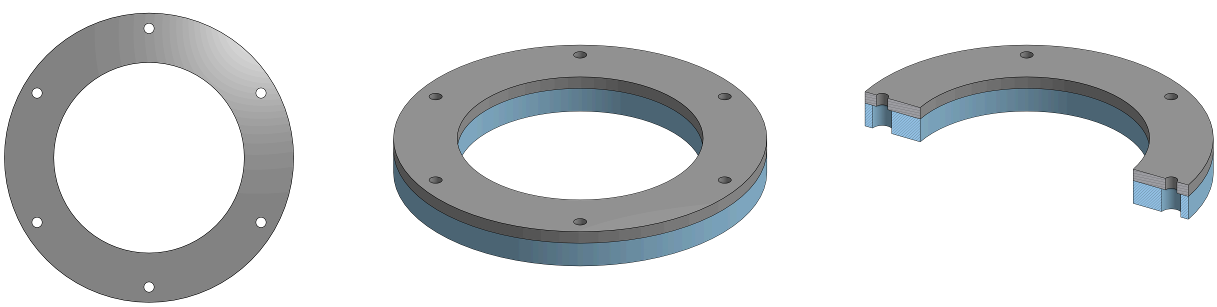

(a) Top view (b) Isometric view (c) Cross-sectional isometric view

Fig. 3 The existing fixture, consisting of two clamping rings that secure the sample, as shown from various angles.

Centrally, our new design allowed for two independently clamped films to be fixtured in contact. Previously, this was infeasible because the existing fixture's clamping rings obstructed contact. In the new design, the rings clamped the edge of the sample at an angle of 7°, mitigating warping resultant from a more extreme angle. Independent symmetric fixtures were then conjoined with screws penetrating through tabs along the edges of the base piece, resulting in contact between the thin-film samples. With these alterations, both identified design objectives were met: *LDV scans could be performed on (1) samples under tension and (2) separately clamped samples (either tensioned or untensioned) in contact*.

Digital Image Correlation (DIC)

Strain quantification in the films was infeasible using physical instrumentation like strain gauges. Digital image correlation (DIC) was explored as an alternative, using the Ncorr MATLAB method [25]. Each film sample was speckled with spray paint, with image capture before and after tensioning to perform 2D DIC analysis. Image capture was as consistent as possible: any difference between current and reference images would be interpreted as deformation by the DIC algorithm,

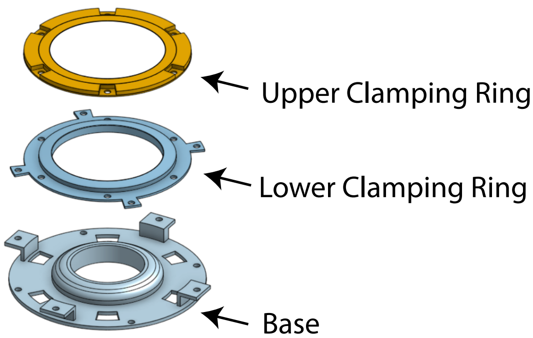

Fig. 4 Exploded view of the experimental fixture.

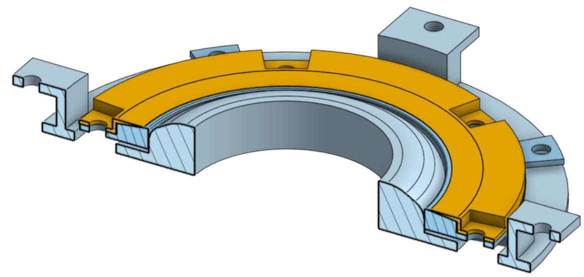

Fig. 5 Cross-sectional view of the experimental fixture.

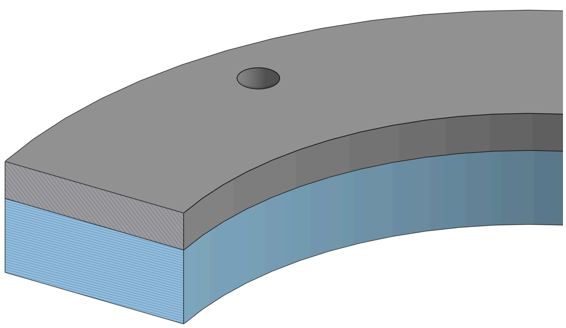

Fig. 6 Cross-sectional view of Gen 0 (initial fixture).

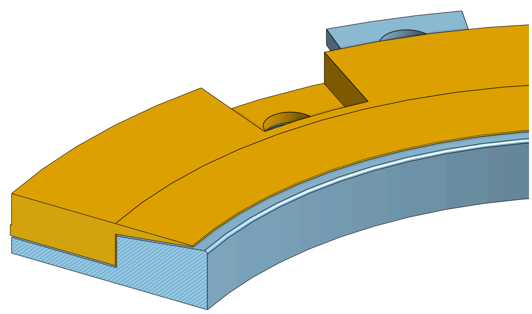

Fig. 7 Cross-sectional view of the clamping rings for Gen 4, showing angled clamping.

which calculated transformation for subsets within the Region Of Interest (ROI). DIC camera was mounted on a tripod, and fixture with the sample was mounted on a small 3D-printed stand (Fig. 8), placed in the same orientation before and after tensioning. Camera height was adjusted so the ROI filled a majority of the frame, maximizing resolution.

Fig. 8 Set-up for image capture for DIC. A camera on a tripod was used to photograph the polymer with fine speckled pattern.

DIC reference image was the sample image before tensioning, and ROI was the sample within the inner diameter of the base piece. ROI was chosen because the deformation in this region can be reasonably assumed to be 2D; if the ROI included the edge of the sample, which lay at an angle when tensioned, the change in angle would be misinterpreted by the algorithm as a 2D deformation. Furthermore, the only strain of interest was in the stretched region under vibroacoustic observation.

Strain was calculated from DIC displacements, by a least squares plane fit over displacement data for a window of sampled points in the ROI [25]. Because the strain calculation involves differentiation, a small strain window will result in a noisy strain field. Strain window size was increased until minimum and maximum strains converged, yielding a smoothing effect.

FEA Model

FEA was formulated in MOOSE using PETSc for eigensystem solution [26], with visualization in Paraview. FEA was based on the mathematical model that was discussion in Sec. . The mathematical model was implemented as cantilever beam, pretensioned circular membrane, and circular plate, and verified with the theoretical solution. For the model of pretensioned circular membrane, circular plate, and the thin film model, the boundary conditions were clamped which were assumed to be fixed. As particularly illustrative for the related optimization task, only circular plate verification is detailed.

For the circular plate verification [27], classically the transverse (*i.e.*, out-of-plane) displacement of a plate is described by a biharmonic equation written in the "flexural modulus,"

$$D = \frac{Eh^3}{12(1-\nu^2)}, \tag{13}$$

where E is the Young's modulus, h is the thickness, and ν is the Poisson ratio. Material is understood to have density ρ. The boundary of the circular plate is permanently clamped at its outer radius a. The j^{th} natural frequency is:

$$\lambda_j^2 = \omega_j a^2 \sqrt{\frac{\rho h}{D}} \quad \Rightarrow \quad \lambda_j^4 = \underbrace{\omega_j^2}_{=f_j} a^4 \left(\frac{\rho h}{D}\right) \tag{14}$$

such that, by Eq. (13),

$$f_1 = \frac{\lambda_1^4 D}{a^4 \rho h} = \frac{\lambda_1^4 h^2}{12 a^4 \rho}\left(\frac{E}{1-\nu^2}\right) \tag{15}$$

where a is the radius of circular plate. λ_1 is the coefficient constant for the 1^{st} natural frequency with $\lambda_1^2 = 10.21$.

Optimization

Our optimization algorithm is investigated in two case studies: a nonconvex problem to directly optimize material properties vs. a convex problem to optimize projected parameters as a mapping of material properties. To validate the optimization algorithm with simulated noise, six target frequencies $f_j \in \boldsymbol{f}$ were obtained via FEA provided target parameters, $\boldsymbol{\theta}$, adding Gaussian noise (with variance one-tenth of the resonant frequency). Fig. 9 shows distribution of $f_j \in \boldsymbol{f}$.

Predicted frequencies, each $\widehat{f}_i$, were obtained from FEA-based determination of predicted parameters, $\widehat{\boldsymbol{\theta}}$, obtained from PyTorch Adam optimization. If the optimization problem is strictly convex, target $\boldsymbol{\theta}$ will match the unique global minimum solution for prediction $\widehat{\boldsymbol{\theta}}$.

Case Study 1: Nonconvex Problem

In the first case study, the goal is to optimize the material parameters directly. Let m and n be number of samples and number of considered resonant frequencies. Define the loss function as

$$L_1 = \frac{1}{m}\sum_{i=1}^{m}\sum_{j=1}^{n}\left(A_{jj}^{(i)}\left(f_j^{(i)} - \widehat{f}_j\right)\right)^2 \tag{16}$$

where $f_j^{(i)}$ is the j^{th} component (resonant frequency) of the i^{th} sample, and normalization matrix $A^{(i)}$ is

$$A_{jk}^{(i)} = \begin{cases} \frac{1}{f_j^{(i)}} & \text{when } j = k \\ 0 & \text{when } j \neq k. \end{cases} \tag{17}$$

$A^{(i)}$ is applied to weight each resonant frequency equally in the loss function: mentioned in Sec. , the 1^{st} resonant frequency is nearly four times smaller than the 6^{th} resonant frequency.

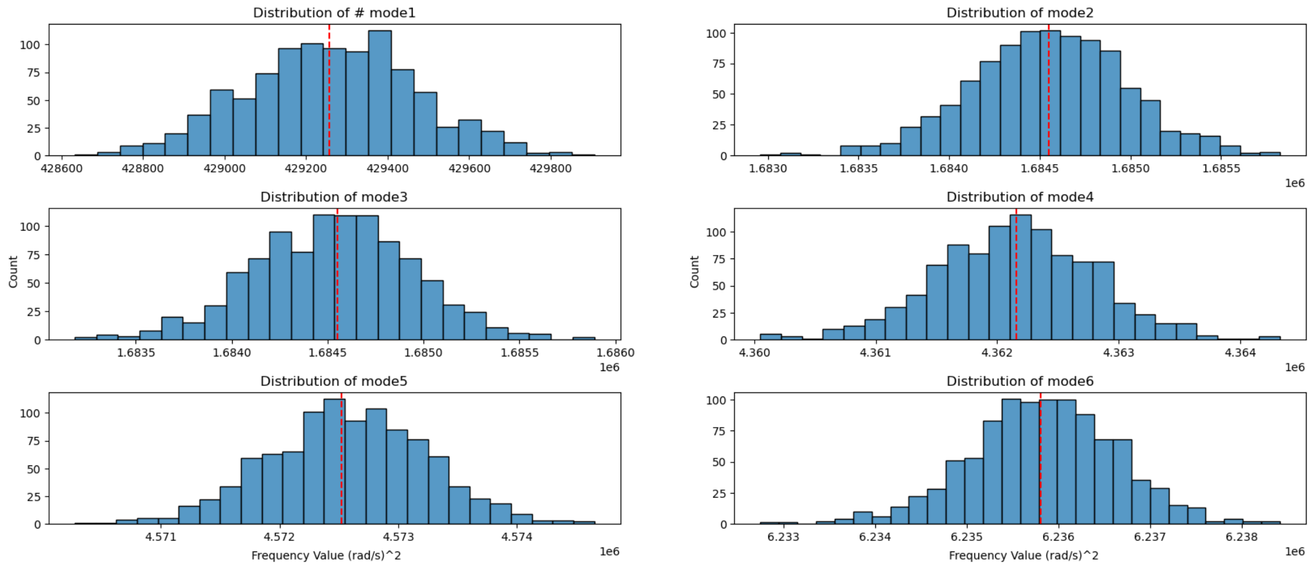

Fig. 9 Distribution of the 1st six resonant frequencies. The red line presents the outputted resonant frequency from the target model. The histogram shows the distribution of the frequency after adding Gaussian noise to form 1000 samples.

A FEA forward pass obtains $\widehat{\boldsymbol{f}}$ given $\widehat{\boldsymbol{\theta}}$. Let $\widehat{\boldsymbol{X}}$ represent PyTorch optimization variables, and let $\mathbf{C}$ represent scaling from $\widehat{\boldsymbol{X}}$ to FEA parameters $\widehat{\boldsymbol{\theta}}$. Their relation is written as

$$\widehat{\boldsymbol{\theta}} = \mathbf{C}\widehat{\boldsymbol{X}} = \begin{bmatrix} c_1 & 0 \\ 0 & c_2 \end{bmatrix} \begin{bmatrix} x_1 \\ x_2 \end{bmatrix} = \begin{bmatrix} c_1 x_1 \\ c_2 x_2 \end{bmatrix}. \tag{18}$$

Since optimized via gradient descent (*i.e.*, in order to use FEA result $\widehat{\boldsymbol{f}}$ to update $\widehat{\boldsymbol{\theta}}$), the loss function's gradient is needed:

$$\frac{\partial L}{\partial \widehat{\boldsymbol{X}}} = \frac{\partial L}{\partial \widehat{\boldsymbol{f}}} \frac{\partial \widehat{\boldsymbol{f}}}{\partial \widehat{\boldsymbol{X}}}. \tag{19}$$

$\partial L / \partial \widehat{\boldsymbol{f}}$, viable to express analytically, is *computed by PyTorch Autograd*. Conversely, as $\widehat{\boldsymbol{f}}$ is output from the FEA forward pass, the latter matrix-valued partial derivative is computed by finite differencing of FEA with step size h:

$$\frac{\partial \widehat{\boldsymbol{f}}}{\partial \widehat{X}_j} = \frac{\boldsymbol{f}(c_j(\widehat{X}_j + h)) - \boldsymbol{f}(c_j(\widehat{X}_j - h))}{2h} \tag{20}$$

where $\boldsymbol{f}(\cdot)$ represents the frequency vector resultant from FEA. The gradient is used to update $\widehat{\boldsymbol{X}}$ until optimality.

In this case study, the target model is parameterized by shear modulus, G, bulk modulus, K, and density, ρ. Since ρ is assumed to be known, $G, K \in \boldsymbol{\theta}$. The goal is to find optimized $\widehat{G}, \widehat{K} \in \widehat{\boldsymbol{\theta}}$ yielding the minimum loss function. However, this optimization problem is not strictly convex: optimization may give a possibly non-global minimizer $\widehat{\boldsymbol{\theta}}$, as shown in Sec. , different from true $\boldsymbol{\theta}$. To address this issue, $\boldsymbol{\theta}$ is mapped to describe a strictly convex optimization problem with a unique, global minimum.

Case Study 2: Convex Problem

In Sec. , the optimization problem was not strictly convex lacking a unique global solution. In order to reform the loss function as convex, an appropriate mapping to $\boldsymbol{\theta}$ should be selected. From Eq. (15), the 1st resonant frequency was linear w.r.t $E/(1-\nu^2)$. Elastic modulus E and Poisson's ratio ν could be related to Lamé's constant λ and P-wave modulus M, based on the relationship between material properties,

$$E = \frac{(M-\ell)(M+2\ell)}{M+\ell}, \quad \nu = \frac{\ell}{M+\ell}, \quad f_1 = \frac{\lambda^4 h^2}{12 a^4 \rho}\left(-\frac{\ell^2}{M} + M\right). \tag{21}$$

From Eq. (21), the 1st resonant frequency was linear w.r.t ℓ^2/M, and M which can describe target parameters $\boldsymbol{\theta}$. In addition, a penalty term was added to Eq. (16) to ensure strict convexity of the loss function. M_c represented the experimental P-wave modulus, to be obtained from non-destructive experimentation. L_2 optimization's loss function was defined by:

$$L_2 = \frac{1}{m}\sum_{i=1}^{m}\sum_{j=1}^{n}\left[\left(A_{jj}^{(i)}\left(f_j^{(i)} - \widehat{f}_j\right)\right)^2\right] + \frac{k}{2}\left(\widehat{M} - M_c\right)^2. \tag{22}$$

$\widehat{\boldsymbol{X}}$ is the optimization variable such that:

$$\begin{bmatrix} \widehat{\ell}^2/\widehat{M} \\ \widehat{M} \end{bmatrix} = \mathbf{C}\widehat{\boldsymbol{X}} = \begin{bmatrix} c_1 x_1 \\ c_2 x_2 \end{bmatrix}. \tag{23}$$

Assuming $c_1 = c_2 = c > 0$:

$$\widehat{\ell} = \sqrt{\widehat{M} c_1 x_1} = c\sqrt{x_1 x_2}, \quad \widehat{M} = c_2 x_2 = c x_2. \tag{24}$$

Iterative parameters $\widehat{G}, \widehat{\ell} \in \widehat{\boldsymbol{\theta}}$ are defined by:

$$\widehat{\boldsymbol{\theta}} = \begin{bmatrix} \widehat{G} \\ \widehat{\ell} \end{bmatrix} = \begin{bmatrix} (\widehat{M} - \widehat{\ell})/2 \\ \widehat{\ell} \end{bmatrix} = c\begin{bmatrix} (x_2 - \sqrt{x_1 x_2})/2 \\ \sqrt{x_1 x_2} \end{bmatrix}. \tag{25}$$

The optimization algorithm is shown in Algorithm 1.

Algorithm 1 Parameter optimization with FEA

1: **Input:** target frequency $\boldsymbol{f}$, scaling constant $\mathbf{C}$, experimental P-wave modulus M_c, penalty constant k, step-size h, tolerance ε_t, learning rate γ
2: Initialize variables: $\widehat{\boldsymbol{X}}_t$
3: **while** $\Delta L_2 > \varepsilon_t$ **do**
4: Compute variable transformation: $\widehat{\boldsymbol{X}}_t \Rightarrow \widehat{\boldsymbol{\theta}}_t$
5: Execute FEA with iterative parameters, $\widehat{\boldsymbol{\theta}}_t$, to compute predicted resonant frequencies, $\widehat{\boldsymbol{f}}$
6: Compute $L_2(\widehat{\boldsymbol{X}}_t)$ as Eq. (22)
7: Execute FEA to compute $\partial\widehat{\boldsymbol{f}}/\partial\widehat{\boldsymbol{X}}$ as Eq. (20)
8: Compute $\partial L_2/\partial\widehat{\boldsymbol{X}}$
9: Update $\widehat{\boldsymbol{X}}_{t+1}$ by Adam optimizer
10: Compute $\Delta L_2 = L_2(\widehat{\boldsymbol{X}}_t)$ - $L_2(\widehat{\boldsymbol{X}}_{t+1})$
11: **end while**
12: **return** Optimal parameters $\widehat{\boldsymbol{X}}$

After the change in iterative parameters and optimization variables, Eq. (22) is strictly convex so the loss function has a unique and global minimum.

Proof: By assuming $n = 1$ in Eq. (22), combining Eq. (15) and Eq. (21) yields (as verified in Sec.) that:

$$\widehat{f}_1 = \frac{\lambda_1^4 h^2}{12a^4\rho}\left(-\frac{\ell^2}{M} + M\right). \tag{26}$$

The Hessian matrix of L_2 with assumption of $n = 1$:

$$\mathbf{H} = \begin{bmatrix} \frac{\partial^2 L_2}{\partial x_1^2} & \frac{\partial^2 L_2}{\partial x_1 x_2} \\ \frac{\partial^2 L_2}{\partial x_2 x_1} & \frac{\partial^2 L_2}{\partial x_2^2} \end{bmatrix} = \begin{bmatrix} 2\left(A_{11}^{(i)}\right)^2\left(\frac{\lambda_1^4 h^2 c}{12a^4\rho}\right)^2 & -2\left(A_{11}^{(i)}\right)^2\left(\frac{\lambda_1^4 h^2 c}{12a^4\rho}\right)^2 \\ -2\left(A_{11}^{(i)}\right)^2\left(\frac{\lambda_1^4 h^2 c}{12a^4\rho}\right)^2 & 2\left(A_{11}^{(i)}\right)^2\left(\frac{\lambda_1^4 h^2 c}{12a^4\rho}\right)^2 + kc^2 \end{bmatrix}. \tag{27}$$

If $\mathbf{H}$ is positive definite, the loss function will be strictly convex. $\mathbf{H}$ is positive definite if and only if $\mathbf{H}$ is symmetric and all its eigenvalues are real and positive. As $\mathbf{H}$ is symmetric and real-valued, its eigenvalues are also real-valued. Assuming the product of $\mathbf{H}$'s eigenvalues, $\det\mathbf{H} > 0$, its eigenvalues are either both positives or both negative. To eliminate the possibility of both negative eigenvalues, $\mathbf{z}\mathbf{H}\mathbf{z}^{\mathrm{T}} \not< 0$ must be satisfied for arbitrary $\mathbf{z}$. But $\mathbf{z}\mathbf{H}\mathbf{z}^{\mathrm{T}} \not< 0$ satisfies when $\mathbf{z} = \begin{bmatrix} 1 & 0 \end{bmatrix}$ because

$$H_{11} = 2(A_{11}^{(i)})^2(\lambda_1^4 h^2 c)^2/(12a^4\rho)^2 > 0,$$

and both eigenvalues must be positive. Thus, $\mathbf{H}$ is positive definite as

$$\det\mathbf{H} = \left(2\left(A_{11}^{(i)}\right)^2\left(\frac{\lambda_1^4h^2c}{12a^4\rho}\right)^2\right)\left(2\left(A_{11}^{(i)}\right)^2\left(\frac{\lambda_1^4h^2c}{12a^4\rho}\right)^2+kc^2\right)-\left(2\left(A_{11}^{(i)}\right)^2\left(\frac{\lambda_1^4h^2c}{12a^4\rho}\right)^2\right)^2 = 2k\left(A_{11}^{(i)}\right)^2\left(\frac{\lambda_1^4h^2c^2}{12a^4\rho}\right)^2,$$

which is positive if and only if $k > 0$ (as required). Summarizing:

$$L_2 \text{ has a unique global minimum} \Leftrightarrow L_2 \text{ is strictly convex} \Leftrightarrow \mathbf{H} \text{ is positive definite} \Leftrightarrow \det\mathbf{H} > 0 \Leftrightarrow k > 0. \tag{28}$$

Results

Using an initial fixture design shown in Fig. 3, LDV was conducted on two samples of the same material (PVDF 254 μm). The correlation coefficient for the two datasets was 0.71. The 1$^{\text{st}}$ resonant frequency occurs near 500 Hz for both samples, as visualization of the velocity across the sample confirmed peaks at lower frequencies to result from noise. Discrepancy exists between the location of this 1$^{\text{st}}$ peak (and later peaks as well), even between two samples of the same material.

Using the redesigned fixture, LDV scans were conducted on two samples of the same material (PVDF 254 μm). Fig. 11 shows the results when no tension is applied to the sample. Results are plotted on a log scale. Correlation coefficient for this

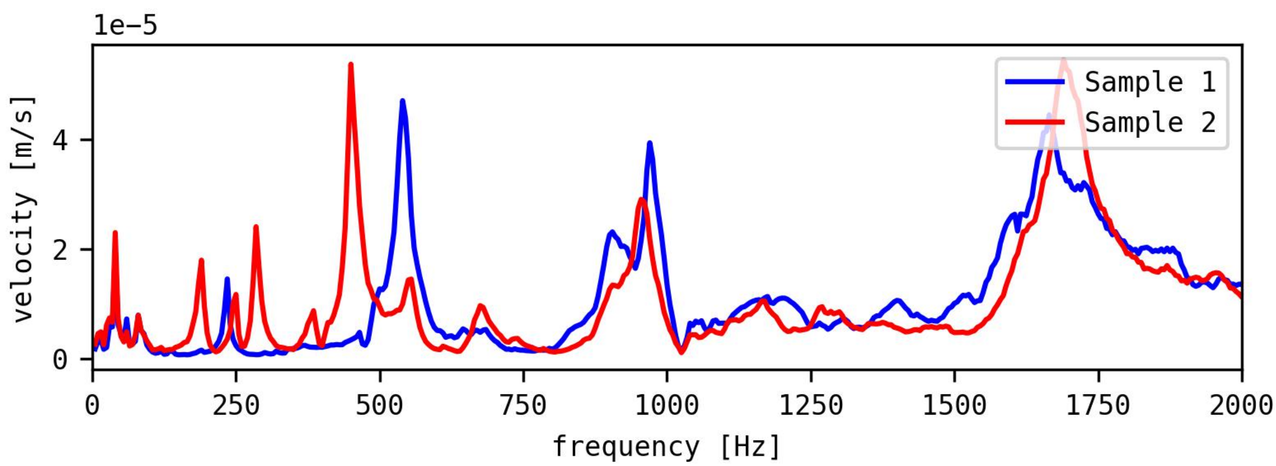

Fig. 10 Correlation coefficient was 0.71 for two samples of the same material when tested with the initial fixture.

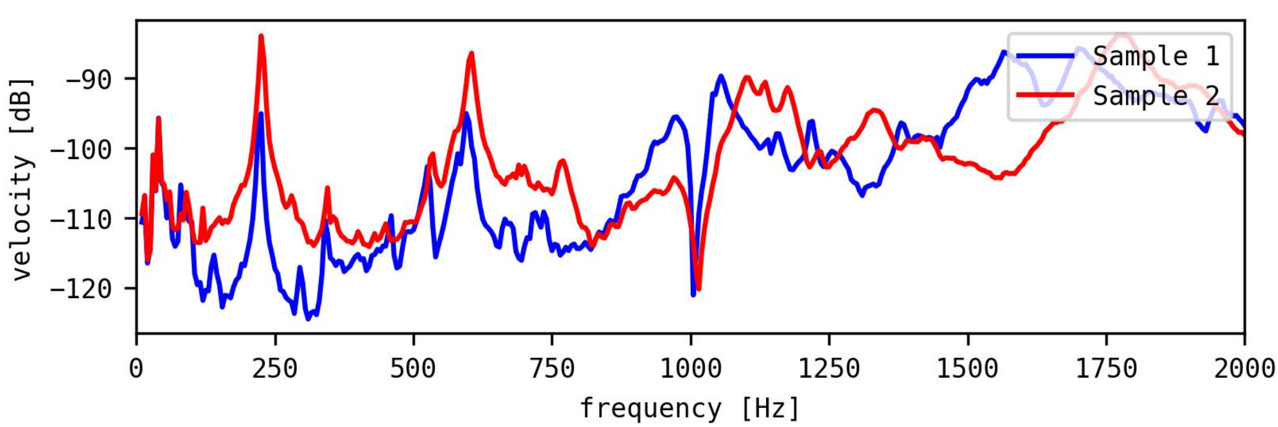

Fig. 11 Correlation coefficient was 0.71 for two samples of the same material when tested with the redesigned fixture and no tension was applied.

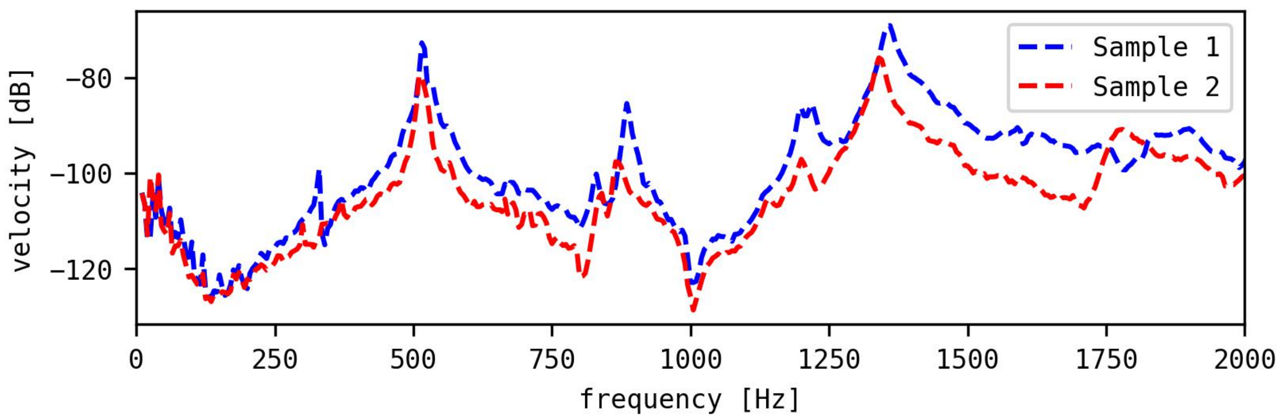

Fig. 12 Correlation coefficient was 0.93 for two samples of the same material when tested with the redesigned fixture and tension was applied.

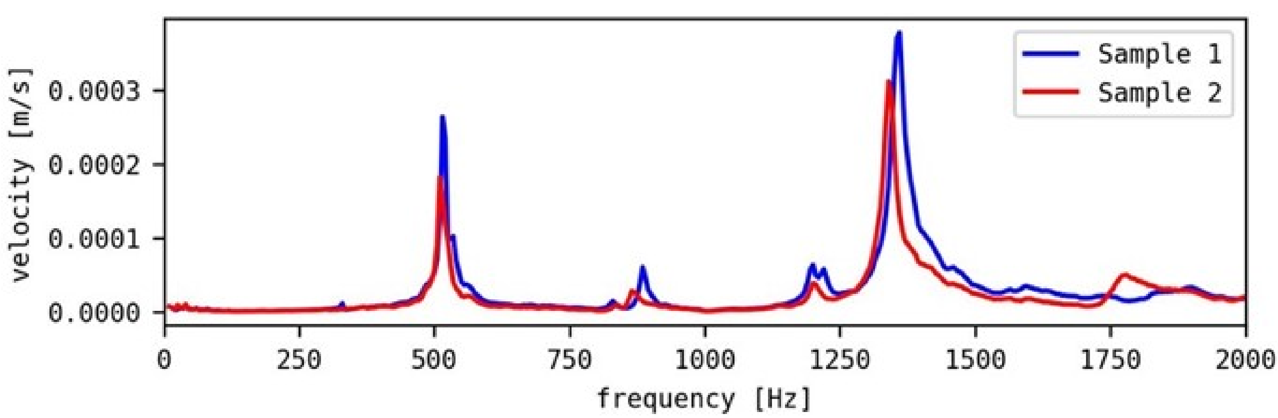

Fig. 13 Correlation coefficient was 0.81 for two samples of the same material when tested with the redesigned fixture and tension was applied.

data was found to be 0.71. Then, tension was applied to both samples. Distance between the clamping rings and the base piece, which controls the level of tension, was a uniform value of 0.1 inches for both samples. LDV scans were reconducted, and results are shown (with a log scale) in Fig. 12. Correlation coefficient in the tensioned case was found to be 0.93. As a baseline, tension was applied to two samples of PVDF 254 μm, with seperate data collection for each. Correlation was 0.81, and results are shown in Figure 13. This correlation coefficient differs to the results in Fig. 12, though the experiment was of the same nature. When these two films were held in contact by attaching the two fixtures to each other, and data was collected again, correlation increased. Correlation coefficient was 0.99, as seen in Fig. 14.

DIC

Sample 1 and sample 2 were both analyzed with DIC. Sample 1 showed a maximum strain of 0.10% in the *x*-direction and 0.10% in the *y*-direction, as shown in Fig. 15. Sample 2 showed a maximum strain of 0.23% in the *x*-direction and 0.18% in the *y*-direction, as shown in Fig. 16. Maximum strain in the *x*-direction occurred at the leftmost or rightmost areas within the ROI for both samples, along the outer edge of the ROI. Likewise, maximum strain in the *y*-direction occurred along the top or bottom edges of the ROI for both samples. In both samples, the minimum value for strain (ε_{xx} and ε_{yy}) is negative, indicative of an actual or perceived contraction.

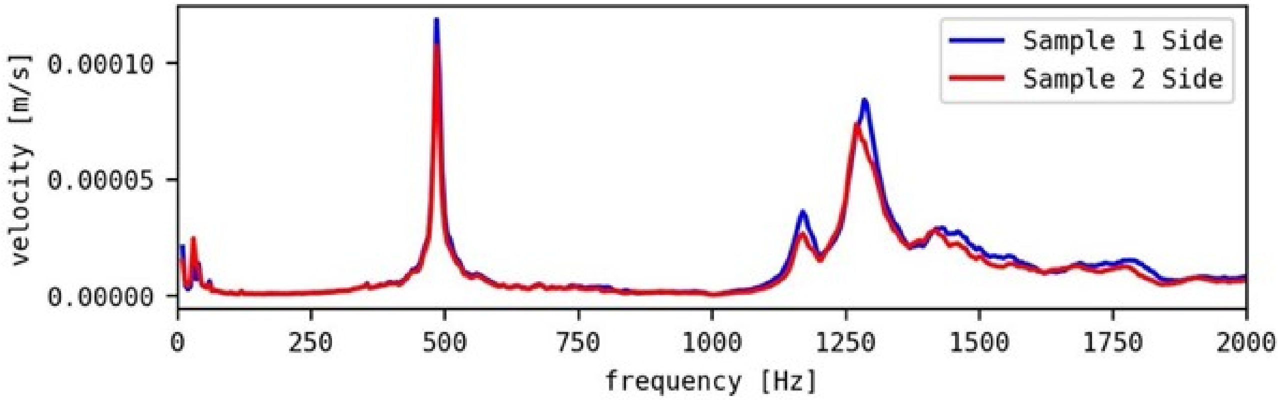

Fig. 14 Correlation coefficient was 0.99 for two samples of the same material held in contact. The films were tested with the redesigned fixture and tension was applied.

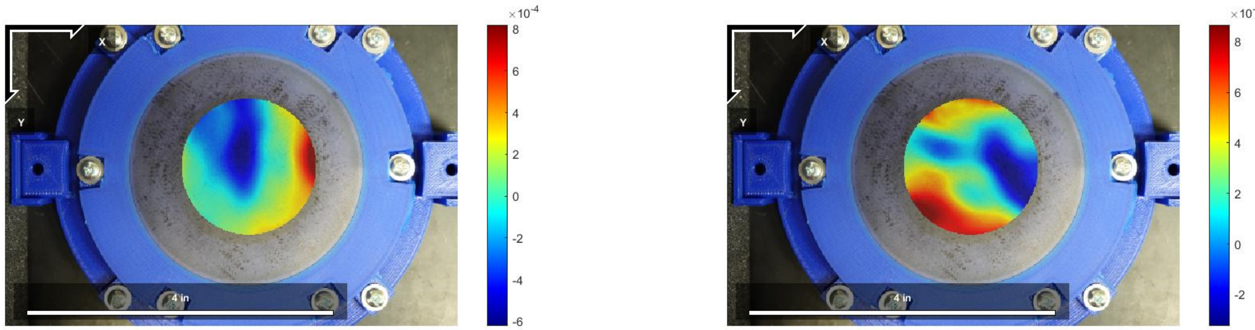

(a) ε_{xx}

(b) ε_{yy}

Fig. 15 Strain fields in Sample 1 after tensioning.

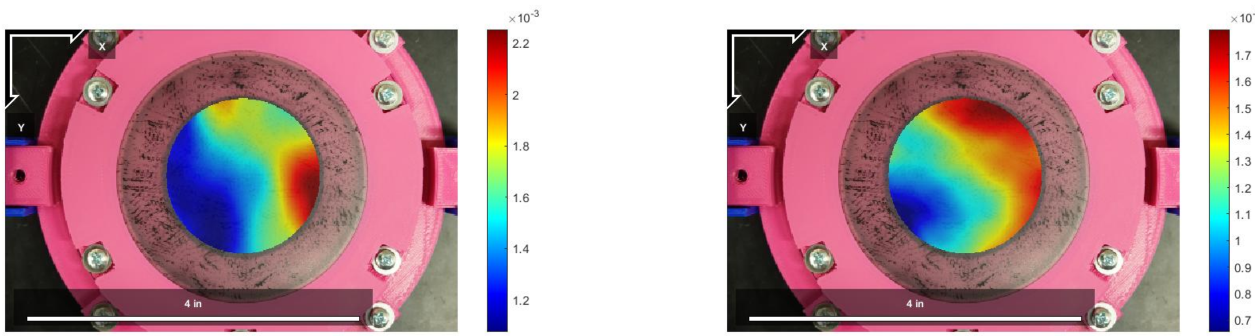

(a) ε_{xx}

(b) ε_{yy}

Fig. 16 Strain fields in Sample 2 after tensioning.

FEA Model

For the clamped circular plate validation model, the modal parameters are shown in Table 1. Comparison of 1st modes between the FE clamped circular plate validation model and Eq. (15) is shown in Table 2. The 1st mode's error between theoretical equation and FEA is 0.05%.

Table 1 Clamped circular plate validation model's modal parameters.

a (m)	h (m)	ρ (kg/m^3)	E (MPa)	ν
200	10	7.8e-9	2.1	0.28

Table 2 1st mode accuracy of circular plate and circular membrane validation model.

Type of Validation	Theoretical Equation (Hz)	Validation FEA (Hz)	Error (%)
Clamped Circular Plate	17.86	17.95	0.05
Clamped Pretensioned Circular Membrane	881	883	0.19

Optimization

The optimization algorithm was examined with 10 random initializations of $\widehat{\boldsymbol{X}}$ from a uniform distribution, $U(0,10)$. The same initialization was used on both case study to demonstrate and validate the difference between the two case studies. For the target model, model parameters and the specific parameters, $\boldsymbol{\theta}$, are shown in Table 3.

Table 3 Target model's model parameters and specific parameters, $\boldsymbol{\theta}$.

a (m)	h (mm)	ρ (kg/m^3)	G (MPa)	ℓ (MPa)	K (MPa)
0.036	0.076	1.45e3	828	7448	8000

Fig. 17 shows convergence iteration results under 10 random initializations. The top plot shows the convergence of the loss function under either L_1 or L_2. The second and the third plots show the convergence of the iterative parameters, $\widehat{\boldsymbol{\theta}}$. Solid line represents the specific parameters, $\boldsymbol{\theta}$, which serve as ground truth. Dashed lines represent iterative parameter values, $\widehat{\boldsymbol{\theta}}$, across iterations. Average of the 10 converged iterative parameters, $\widehat{\boldsymbol{\theta}}$, is shown in Table 4, comparing error w.r.t. $\boldsymbol{\theta}$.

For case study 1 under the L_1 loss function, the average of the 10 converged value of $\widehat{G}$ and $\widehat{K}$ is 970 MPa and 6090 MPa, respectively. Comparing to G and K, the percentage error of $\widehat{G}$ and $\widehat{K}$ is 17.1% and -23.9%, respectively. For case study 2 under the L_2 loss function, the converged value of $\widehat{G}$ and $\widehat{\ell}$ is 829 MPa and 7450 MPa, respectively. Comparing to G and ℓ, the percentage error of $\widehat{G}$ and $\widehat{\ell}$ is 0.12% and 0.03%, respectively.

Table 4 Percentage error of the iterative parameters, $\widehat{\boldsymbol{\theta}}$.

Loss function	K (MPa)	$\widehat{K}$ (MPa, %)	G (MPa)	$\widehat{G}$ (MPa, %)	ℓ (MPa)	$\widehat{\ell}$ (MPa, %)
L_1	8000	6090 (-23.9%)	828	970 (+17.1%)	–	–
L_2	–	–	828	829 (+0.12%)	7448	7450 (+0.03%)

Discussion

LDV scans with the initial fixture show discrepancies in the results for two samples of the same material (Fig. 10). When LDV scans were conducted with the redesigned fixture, the results for two samples of the same material still showed discrepancies (Fig. 11). In both cases, correlation coefficient was equal to 0.71. However, for the case with the redesigned fixture, such discrepancy appeared to come from the amplitude of the peaks rather than the location.

When tension was applied to both samples, LDV scans showed an increase in correlation, with correlation coefficient increasing to 0.93 (Fig. 12). These results indicate that applying a tension to sample of the same material makes the results between the different samples more consistent with one another and likely more repeatable.

In a separate experiment, documented in Fig. 13 and Fig. 14, two films in tension were scanned first separately and then while held in mutual contact. Correlation coefficient increased from 0.81 in the case of separation to 0.99 in the case of contact. This indicates an interaction between films in contact under fixturing: the two films vibrate *en echelon* under acoustic excitation.

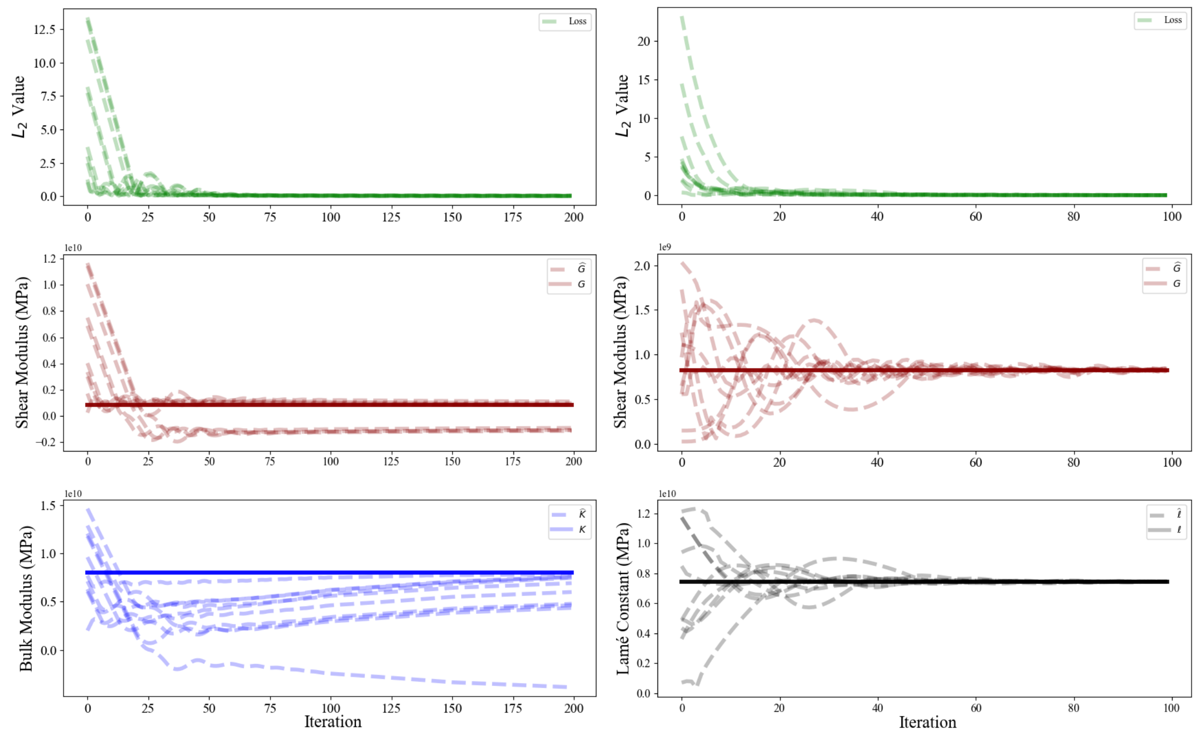

(a) Iteration result under L_1

(b) Iteration result under L_2

Fig. 17 L_1 and L_2 convergence result

DIC

DIC results demonstrated reasonable magnitudes of peak strain. Uncertainties associated with the tensioning include uncertainties in the material of the fixture, uncertainties in the material properties of the two films, and uncertainties associated with the tightening procedure between base piece and clamping pieces. Strains in both samples (Sec.) indicate: the strain in Sample 2 is approximately twice the magnitude of that in Sample 1 in both horizontal and vertical directions. Also, the largest value of maximum strain was found to be 0.23%; since this is less than 2%, the sample is assumed to not undergo plastic deformation.

Additionally, the shape of the strain fields as visualized in Fig. 15 and Fig. 16 are similar. In both samples, the maximum strain in the x-direction occurs along the sides of the sample, and maximum strain in the y-direction occurs along the top or bottom of the sample. This is consistent with what should be expected from a uniform radial strain applied to a circular region. However, a symmetric strain field was expected because applied strain should be uniform throughout the sample. For future work, symmetry would be a promising indication of improved DIC technique.

Uncertainties prevent the use of 2D DIC to fully characterize strain in the sample. For example, the assumption that the sample can be approximated as 2D introduces uncertainty. This assumption is an over-simplification and may account for the negative minimum strain values, which indicate a contraction. Though the contraction is small, it is not negligible as on the same order of magnitude as the maximum strain values. The results indicate that DIC is a reasonable technique for quantifying strain in a sample, but more advanced instrumentation is desirable.

FEA Model

Although the variational principle in Sec. includes interface interaction, the mathematical formulation remains valid for uncoupled solid domains. Table 2 shows error between the theoretical equations and the FEA verification, for benchmarking on single solid domains. Notably (though not detailed herein), error analysis shows that FEA is valid regardless of solid-domain geometry – although cantilever beam flexure significantly differs from circular membrane/plate deformation. Therefore, methods in this study could extend to other applications.

Optimization

Fig. 17 compares convergence of the L_1 and L_2 optimization algorithms. As shown in Fig. 17a, $\widehat{G}$ and $\widehat{K}$ do not converge to the optimal values, G and K, under L_1 optimization with random initialization. Moreover, different initialization leads to different converged values: as L_1 is demonstrably nonconvex, $\widehat{\boldsymbol{\theta}}$ exhibits multiple solutions due to local minima. Indeed, although the L_1 loss function apparently converges, percentage error of average $\widehat{G}$ and $\widehat{K}$ remains more than 15% as shown in Table 4. Given the engineering objective is to determine film flexural properties from experimentation, our results indicate that L_1 optimization is algorithmically inefficient for this purpose.

As shown in Fig. 17b, $\widehat{G}$ and $\widehat{\ell}$ converge to the optimal values, G and ℓ, under the L_2 optimization algorithm with random initialization. Percentage error of the two parameters is less than 0.2% as shown in Table 4. Since L_2 is reformulated for convexity, the loss function numerically exhibits an accurate, unique, and global minimum. Therefore, the L_2 optimization algorithm satisfies the research objective, *i.e.*, to recover the material properties of the tested thin film. The convergence result also indirectly shows alignment between FEA and theoretical formulation. Convexity of L_2 was proved based on the theoretical formulation as shown in Eq. (28). Therefore, FEA preserved the convexity of L_2 indicated by the theoretical formulation.

Conclusion

This study develops novel experimental and FEA-based optimization framework for estimating material parameters of the tested thin films. By the advancement of the fixture design, the thin films can be tested under tension separately and in contact. Meanwhile, the vibration response of thin films becomes more reproducible after tensioning. DIC is used to preliminarily extract initial tensile strains of thin films. FEA precision is verified with the theoretical formulation. The optimization algorithm is also proven with modeled scenarios under random initializations. Overall, this study begins to fill the research gap in the numerical and experimental investigation of thin film vibromorphology, with the following contributions:

- A novel modal parameter optimization framework based on modal response from experiments and numerical models
- Advanced fixture design for repeatable experiment on thin films under tension
- Investigation of tensioning effect on vibroacoustic behavior (vibromorphology)
- Established and verified 3D frequency-domain FEA coupled to PyTorch optimizer
- Reformulated convex optimization algorithm by parameter mapping

Acknowledgments The authors would like to thank Thomas Zane Box and Professor Ricardo Mejia for advising and contributing to the experimental setup, and all the managers and mentors from the 25th Los Alamos Dynamics Summer School for providing resources and hosting the program. This research was funded by Los Alamos National Laboratory (LANL) through the Engineering Institute's Los Alamos Dynamics Summer School. The Engineering Institute is a research and education collaboration between LANL and the University of California San Diego's Jacobs School of Engineering. This collaboration seeks to promote multidisciplinary engineering research that develops and integrates advanced predictive modeling, novel sensing systems, and new developments in information technology to address LANL mission relevant problems.

References

1. Simiao Niu and Zhong Lin Wang. Theoretical systems of triboelectric nanogenerators. *Nano Energy*, 14:161–192, May 2015.
2. Syed Nasimul Alam, Arka Ghosh, Pankaj Shrivastava, Uddeshya Shukla, Kamal Garg, Abhay Chowdary Edara, and Nityananada Sahoo. An introduction to triboelectric nanogenerators. *Nano-Structures & Nano-Objects*, 34:100980, April 2023.
3. Aihua Chen, Chen Zhang, Guang Zhu, and Zhong Lin Wang. Polymer Materials for High-Performance Triboelectric Nanogenerators. *Advanced Science*, 7(14):2000186, 2020.
4. Mina Shanbedi, Haleh Ardebili, and Alamgir Karim. Polymer-based triboelectric nanogenerators: Materials, characterization, and applications. *Progress in Polymer Science*, 144:101723, September 2023.
5. Jianxiong Zhu, Minglu Zhu, Qiongfeng Shi, Feng Wen, Long Liu, Bowei Dong, Ahmed Haroun, Yanqin Yang, Philippe Vachon, Xinge Guo, Tianyiyi He, and Chengkuo Lee. Progress in TENG technology—A journey from energy harvesting to nanoenergy and nanosystem. *EcoMat*, 2(4):e12058, 2020.
6. Yaokun Pang, Yunteng Cao, Masoud Derakhshani, Yuhui Fang, Zhong Lin Wang, and Changyong Cao. Hybrid Energy-Harvesting Systems Based on Triboelectric Nanogenerators. *Matter*, 4(1):116–143, January 2021.
7. Ping Sun, Nixin Cai, Xiaodi Zhong, Xiaojiong Zhao, Lei Zhang, and Saihua Jiang. Facile monitoring for human motion on fireground by using MiEs-TENG sensor. *Nano Energy*, 89:106492, November 2021.

8. Qitao Zhou, Jing Pan, Shujun Deng, Fan Xia, and Taesung Kim. Triboelectric Nanogenerator-Based Sensor Systems for Chemical or Biological Detection. *Advanced Materials*, 33(35):2008276, 2021.
9. Luke B. Beardslee, Marcel C. Remillieux, and T. J. Ulrich. Determining material properties of components with complex shapes using Resonant Ultrasound Spectroscopy. *Applied Acoustics*, 178:108014, July 2021.
10. Yunlong Li, Inkyu Oh, Jiehao Chen, and Yuhang Hu. A new design of dielectric elastomer membrane resonator with tunable resonant frequencies and mode shapes. *Smart Materials and Structures*, 27(6):065029, May 2018.
11. Merve K Ozturk, Klara Kalinova, Banu Nergis, and Cevza Candan. Comparison of resonance frequency of a nanofibrous membrane and a homogeneous membrane structure. *Textile Research Journal*, 83(20):2204–2210, December 2013.
12. M. Kamper and A. Bekker. Non-contact experimental methods to characterise the response of a hyper-elastic membrane. *International Journal of Mechanical and Materials Engineering*, 12(1):15, July 2017.
13. Md Salauddin, R. M. Toyabur, P. Maharjan, M. Salauddin Rasel, Hyunok Cho, and Jae Yeong Park. Design and experimental analysis of a low-frequency resonant hybridized nanogenerator with a wide bandwidth and high output power density. *Nano Energy*, 66:104122, December 2019.
14. Paolo Chiariotti, Christian Rembe, Paolo Castellini, and Matt Allen. Laser Doppler Vibrometry Measurements in Structural Dynamics. In R. Allemang and Peter Avitabile, editors, *Handbook of Experimental Structural Dynamics*, pages 1–45. Springer, New York, NY, 2020.
15. Daria A. Derusova, Vladimir P. Vavilov, Nikolay V. Druzhinin, Victor Y. Shpil'noi, and Alexey N. Pestryakov. Detecting Defects in Composite Polymers by Using 3D Scanning Laser Doppler Vibrometry. *Materials*, 15(20):7176, January 2022.
16. N. B. Roozen, L. Labelle, Q. Leclère, K. Ege, and S. Alvarado. Non-contact experimental assessment of apparent dynamic stiffness of constrained-layer damping sandwich plates in a broad frequency range using a Nd:YAG pump laser and a laser Doppler vibrometer. *Journal of Sound and Vibration*, 395:90–101, May 2017.
17. Shujun Ma, Shiliang Wang, Francesca Iacopi, and Han Huang. A resonant method for determining the residual stress and elastic modulus of a thin film. *Applied Physics Letters*, 103(3):031603, July 2013.
18. Nathaniel M. Roberts and James S. Sharp. Piezoelectric excitation and acoustic detection of thin film polymer membrane vibrations. *Physical Review E*, 109(1):014802, January 2024.
19. R. Huang, J. H. Prévost, Z. Y. Huang, and Z. Suo. Channel-cracking of thin films with the extended finite element method. *Engineering Fracture Mechanics*, 70(18):2513–2526, December 2003.
20. Simiao Niu, Ying Liu, Sihong Wang, Long Lin, Yu Sheng Zhou, Youfan Hu, and Zhong Lin Wang. Theory of Sliding-Mode Triboelectric Nanogenerators. *Advanced Materials*, 25(43):6184–6193, 2013.
21. Jinkai Chen, Junchao Wang, Weipeng Xuan, Shurong Dong, and Jikui Luo. Universal Triboelectric Nanogenerator Simulation Based on Dynamic Finite Element Method Model. *Sensors*, 20(17):4838, January 2020.
22. Zirui Zhao, Xiaoli Wang, Yanqiang Hu, Zhihao Li, and Lizhou Li. Electromechanical modeling for triboelectric nanogenerators considering the distribution of polymer transfer film. *Nano Energy*, 93:106895, March 2022.
23. Subrata Mukherjee. Variational principles in dynamic thermoviscoelasticity. *International Journal of Solids and Structures*, 9(10):1301–1316, October 1973.
24. Diederik P. Kingma and Jimmy Ba. Adam: A Method for Stochastic Optimization, January 2017.
25. J. Blaber, B. Adair, and A. Antoniou. Ncorr: Open-Source 2D Digital Image Correlation Matlab Software. *Experimental Mechanics*, 55(6):1105–1122, July 2015.
26. Guillaume Giudicelli, Alexander Lindsay, Logan Harbour, Casey Icenhour, Mengnan Li, Joshua E. Hansel, Peter German, Patrick Behne, Oana Marin, Roy H. Stogner, Jason M. Miller, Daniel Schwen, Yaqi Wang, Lynn Munday, Sebastian Schunert, Benjamin W. Spencer, Dewen Yushu, Antonio Recuero, Zachary M. Prince, Max Nezdyur, Tianchen Hu, Yinbin Miao, Yeon Sang Jung, Christopher Matthews, April Novak, Brandon Langley, Timothy Truster, Nuno Nobre, Brian Alger, David Andrš, Fande Kong, Robert Carlsen, Andrew E. Slaughter, John W. Peterson, Derek Gaston, and Cody Permann. 3.0 - MOOSE: Enabling massively parallel multiphysics simulations. *SoftwareX*, 26:101690, 2024.
27. Arthur W. Leissa. Circular plates. Scientific and Technical Information Division, National Aeronautics and Space Administration, 1969.